Simscape Model - Nano Active Stabilization System

Dehaeze Thomas

February 17, 2025

Contents

From last sections:

- Uniaxial: No stiff nano-hexapod (should also demonstrate that here)
- Rotating: No soft nano-hexapod, Decentralized IFF can be used robustly by adding parallel stiffness
- Micro-Station multi body model tuned from a modal analysis
- Multi-body model of a nano-hexapod that can be merged with the multi-body model of the micro-station

In this section:

- Take the model of the nano-hexapod described in previous section (stiffness 1um/N)
- Control kinematics: how the external metrology, the nano-hexapod metrology are used to control the sample's position (Section 1)
- Apply decentralized IFF (Section 2)
- Apply HAC-LAC (Section 3)
  - Check robustness to change of payload and to spindle rotation
  - Simulation of experiments
- Conclusion of the conceptual phase, validation with simulations

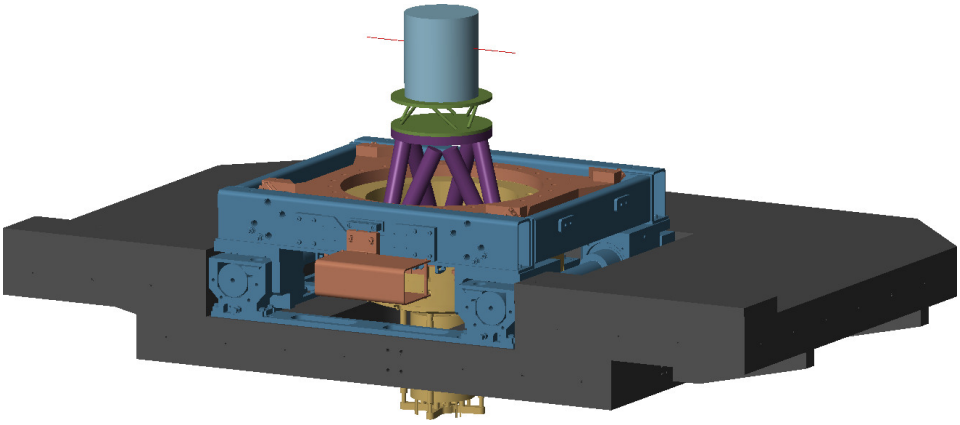

Figure 1: 3D view of the NASS multi-body model

1 Control Kinematics

Figure 1.1 presents a schematic overview of the NASS. This section focuses specifically on the components of the "Instrumentation and Real-Time Control" block.

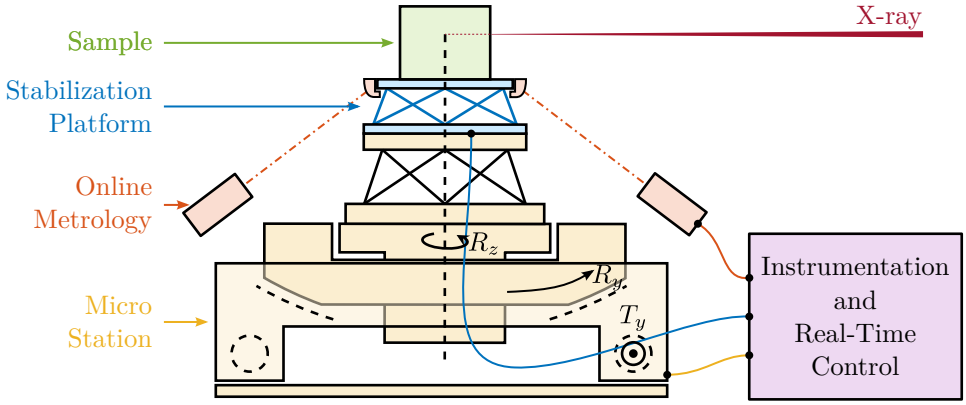

Figure 1.1: Schematic of the Nano Active Stabilization System

As established in the previous section on Stewart platforms, the proposed control strategy combines Decentralized Integral Force Feedback with a High Authority Controller performed in the frame of the struts.

For the Nano Active Stabilization System, computing the positioning errors in the frame of the struts involves three key steps. First, the system computes the desired sample pose relative to a frame representing the point where the X-ray light is focused using micro-station kinematics, as detailed in Section 1.1. Second, it measures the actual sample pose relative to the same fix frame, described in Section 1.2. Finally, it determines the sample pose error and maps these errors to the nano-hexapod struts, as explained in Section 1.3.

The complete control architecture is detailed in Section 1.4.

1.1 Micro Station Kinematics

The micro-station kinematics enables the computation of the desired sample pose from the reference signals of each micro-station stage. These reference signals consist of the desired lateral position r_{D_y}, tilt angle r_{R_y}, and spindle angle r_{R_z}. The micro-hexapod pose is defined by six parameters: three translations $(r_{D_{\mu x}}, r_{D_{\mu y}}, r_{D_{\mu z}})$ and three rotations $(r_{\theta_{\mu x}}, r_{\theta_{\mu y}}, r_{\theta_{\mu z}})$.

Using these reference signals, the desired sample position relative to the fixed frame is expressed through the homogeneous transformation matrix $\boldsymbol{T}_{\mu\text{-station}}$, as defined in equation (1.1).

$$\boldsymbol{T}_{\mu\text{-station}} = \boldsymbol{T}_{D_y} \cdot \boldsymbol{T}_{R_y} \cdot \boldsymbol{T}_{R_z} \cdot \boldsymbol{T}_{\mu\text{-hexapod}} \tag{1.1}$$

$$\begin{aligned}
\boldsymbol{T}_{D_y} &= \begin{bmatrix} 1 & 0 & 0 & 0 \\ 0 & 1 & 0 & r_{D_y} \\ 0 & 0 & 1 & 0 \\ 0 & 0 & 0 & 1 \end{bmatrix} \quad \boldsymbol{T}_{\mu\text{-hexapod}} = \left[\begin{array}{ccc|c} & \boldsymbol{R}_x(r_{\theta_{\mu x}})\boldsymbol{R}_y(r_{\theta_{\mu y}})\boldsymbol{R}_z(r_{\theta_{\mu z}}) & & \begin{matrix} r_{D_{\mu x}} \\ r_{D_{\mu y}} \\ r_{D_{\mu z}} \end{matrix} \\ \hline 0 & 0 & 0 & 1 \end{array}\right] \\
\boldsymbol{T}_{R_z} &= \begin{bmatrix} \cos(r_{R_z}) & -\sin(r_{R_z}) & 0 & 0 \\ \sin(r_{R_z}) & \cos(r_{R_z}) & 0 & 0 \\ 0 & 0 & 1 & 0 \\ 0 & 0 & 0 & 1 \end{bmatrix} \quad \boldsymbol{T}_{R_y} = \begin{bmatrix} \cos(r_{R_y}) & 0 & \sin(r_{R_y}) & 0 \\ 0 & 1 & 0 & 0 \\ -\sin(r_{R_y}) & 0 & \cos(r_{R_y}) & 0 \\ 0 & 0 & 0 & 1 \end{bmatrix}
\end{aligned} \tag{1.2}$$

1.2 Computation of the sample's pose error

The external metrology system measures the sample position relative to the fixed granite. Due to the system's symmetry, this metrology provides measurements for five degrees of freedom: three translations (D_x, D_y, D_z) and two rotations (R_x, R_y).

The sixth degree of freedom (R_z) is still required to compute the errors in the frame of the nano-hexapod struts (i.e. to compute the nano-hexapod inverse kinematics). This R_z rotation is estimated by combining measurements from the spindle encoder and the nano-hexapod's internal metrology, which consists of relative motion sensors in each strut (note that the micro-hexapod is not used for R_z rotation, and is therefore ignore for R_z estimation).

The measured sample pose is represented by the homogeneous transformation matrix $\boldsymbol{T}_{\text{sample}}$, as shown in equation (1.3).

$$\boldsymbol{T}_{\text{sample}} = \left[\begin{array}{ccc|c} & \boldsymbol{R}_x(R_x)\boldsymbol{R}_y(R_y)\boldsymbol{R}_z(R_z) & & \begin{matrix} D_x \\ D_y \\ D_z \end{matrix} \\ \hline 0 & 0 & 0 & 1 \end{array}\right] \tag{1.3}$$

1.3 Position error in the frame of the struts

The homogeneous transformation formalism enables straightforward computation of the sample position error. This computation involves the previously computed homogeneous 4×4 matrices: $\boldsymbol{T}_{\mu\text{-station}}$ representing the desired pose, and $\boldsymbol{T}_{\text{sample}}$ representing the measured pose. Their combination yields $\boldsymbol{T}_{\text{error}}$, which expresses the position error of the sample in the frame of the rotating nano-hexapod, as shown in equation (1.4).

$$\boldsymbol{T}_{\text{error}} = \boldsymbol{T}_{\mu\text{-station}}^{-1} \cdot \boldsymbol{T}_{\text{sample}} \tag{1.4}$$

The known structure of the homogeneous transformation matrix facilitates efficient real-time computation of the inverse. From $\boldsymbol{T}_{\text{error}}$, the position and orientation errors $\boldsymbol{\epsilon}_{\mathcal{X}} = [\epsilon_{D_x},\ \epsilon_{D_y},\ \epsilon_{D_z},\ \epsilon_{R_x},\ \epsilon_{R_y},\ \epsilon_{R_z}]$ of the sample are extracted using equation (1.5):

$$
\begin{aligned}
\epsilon_{D_x} &= \boldsymbol{T}_{\text{error}}(1,4) \\
\epsilon_{D_y} &= \boldsymbol{T}_{\text{error}}(2,4) \\
\epsilon_{D_z} &= \boldsymbol{T}_{\text{error}}(3,4) \\
\epsilon_{R_y} &= \text{atan2}(\boldsymbol{T}_{\text{error}}(1,3), \sqrt{\boldsymbol{T}_{\text{error}}(1,1)^2 + \boldsymbol{T}_{\text{error}}(1,2)^2}) \\
\epsilon_{R_x} &= \text{atan2}(-\boldsymbol{T}_{\text{error}}(2,3)/\cos(\epsilon_{R_y}), \boldsymbol{T}_{\text{error}}(3,3)/\cos(\epsilon_{R_y})) \\
\epsilon_{R_z} &= \text{atan2}(-\boldsymbol{T}_{\text{error}}(1,2)/\cos(\epsilon_{R_y}), \boldsymbol{T}_{\text{error}}(1,1)/\cos(\epsilon_{R_y}))
\end{aligned}
\tag{1.5}
$$

Finally, these errors are mapped to the strut space through the nano-hexapod Jacobian matrix (**??**).

$$
\boldsymbol{\epsilon}_{\mathcal{L}} = \boldsymbol{J} \cdot \boldsymbol{\epsilon}_{\mathcal{X}} \tag{1.6}
$$

1.4 Control Architecture

The complete control architecture is summarized in Figure 1.2. The sample pose is measured using external metrology for five degrees of freedom, while the sixth degree of freedom (Rz) is estimated by combining measurements from the nano-hexapod encoders and spindle encoder.

The sample reference pose is determined by the reference signals of the translation stage, tilt stage, spindle, and micro-hexapod. Position error computation follows a two-step process: first, homogeneous transformation matrices are used to determine the error in the nano-hexapod frame, then the Jacobian matrix $\boldsymbol{J}$ maps these errors to individual strut coordinates.

For control purposes, force sensors mounted on each strut are used in a decentralized way for active damping, as detailed in Section 2. Then, the high authority controller uses the computed errors in the frame of the struts to provides real-time stabilization of the sample position (Section 3).

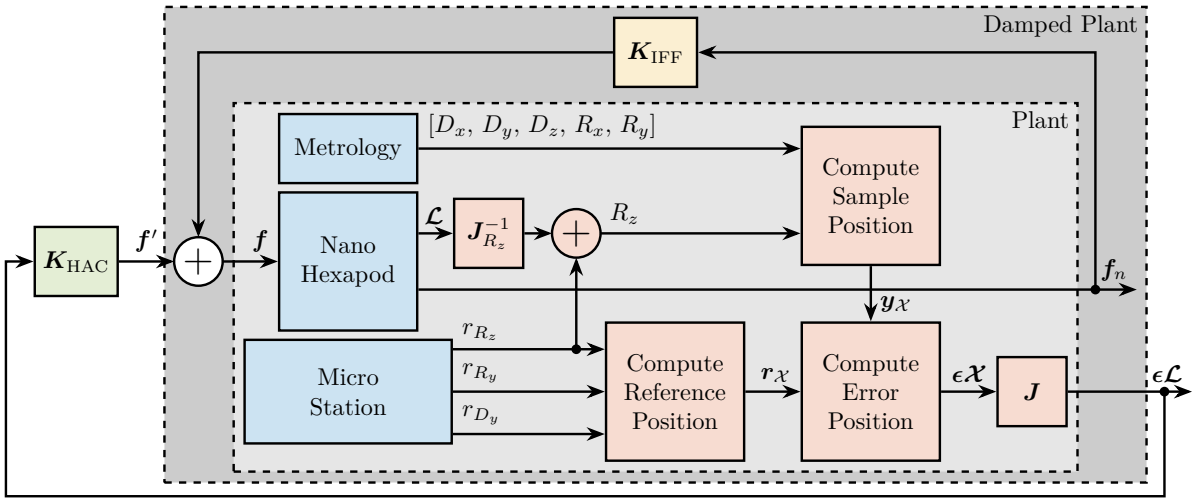

Figure 1.2: The physical systems are shown in blue, the control kinematics in red, the decentralized Integral Force Feedback in yellow and the centralized High Authority Controller in green.

2 Decentralized Active Damping

- How to apply/optimize IFF on an hexapod?
- Robustness to payload mass
- Root Locus
- Damping optimization

Explain which samples are tested:

- cylindrical, 250mm height
- mass of 1kg, 25kg and 50kg

2.1 IFF Plant

Using the multi-body model, the transfer functions from the six actuator forces f_i to the six force sensors f_{mi} are computed.

First the effect of added parallel stiffness on the plant dynamics is studied in Figure 2.1. The plant is identified while the Spindle is rotating at a maximum velocity $\Omega_z = 360\,\text{deg/s}$. The payload mass is 25kg. The obtained dynamics without the parallel stiffness (Figure 2.1a) has non-minimum phase zeros at low frequency, as was predicted using the 3-DoF rotating model. When the parallel stiffness is added (Figure 2.1b), a minimum phase complex conjugate zero is obtained instead, which permits to use decentralized IFF with unconditional stability.

In both cases, high coupling around resonances, but should have guaranteed stability thanks to the collocated nature of actuators and sensors.

- Effect of Rotation 2.2a: almost negligible thanks to sufficient actuator stiffness of $1\,\mu m/N$ (determined using the uniaxial model) coupling is increased at much lower frequency that the first mode to damp and should therefore do not impact the control performances
- Effect of payload's mass 2.2b: still have alternating poles and zeros, and therefore bounded phase between 0 and 180 degrees. Location of poles change with the payload's mass as expected.

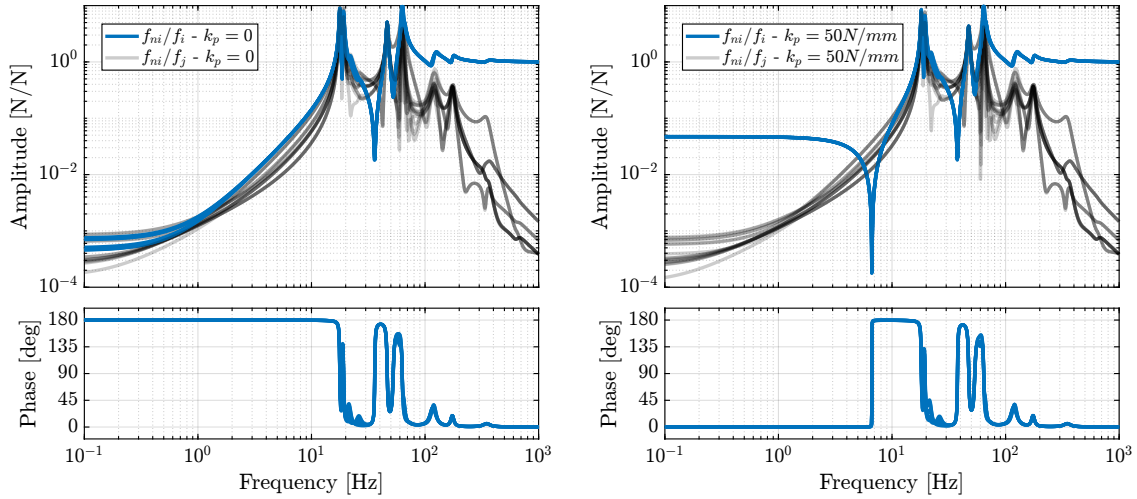

(a) without parallel stiffness **(b)** with parallel stiffness

Figure 2.1: Effect of stiffness parallel to the force sensor on the IFF plant with $\Omega_z = 360\,\text{deg/s}$ and payload mass of 25kg. The dynamics without parallel stiffness has non-minimum phase zeros at low frequency (a). The added parallel stiffness transforms the non-minimum phase zeros to complex conjugate zeros (b)

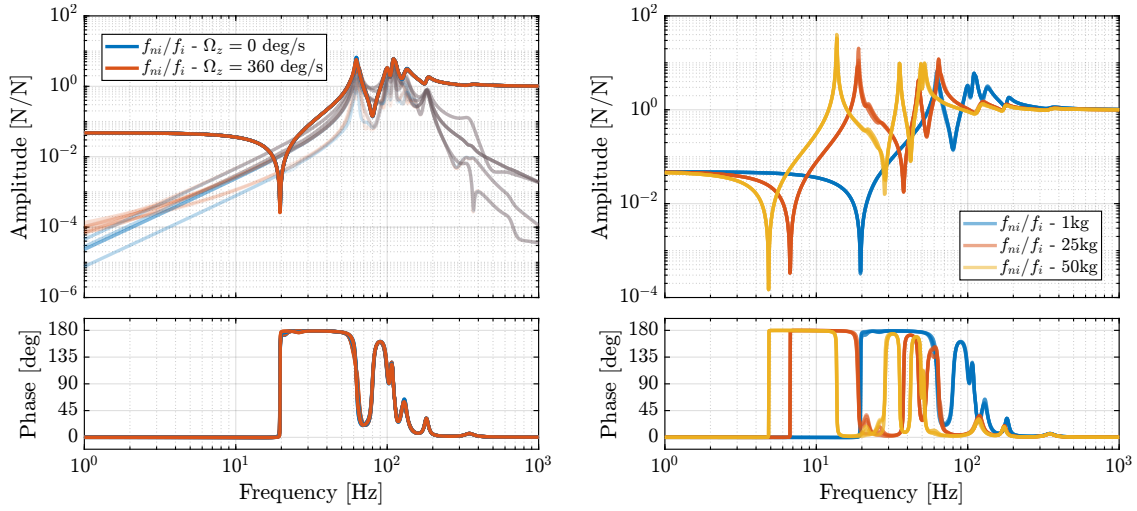

(a) Effect of Spindle rotation **(b)** Effect of payload mass

Figure 2.2: Effect of the Spindle's rotational velocity on the IFF plant (a) and effect of the payload's mass on the IFF plant (b)

2.2 Controller Design

Using the 3DoF rotating model, it was shown that the decentralized IFF with pure integrators becomes unstable due to gyroscopic induced by the spindle's rotation. It was shown that adding sufficient stiffness in parallel with the force sensor allows to make the decentralized IFF unconditional stable again. Such parallel stiffness are here added to the nano-hexapod, and using the multi-body model of the NASS, it is verified that without parallel stiffness, the system would be unstable when using decentralized IFF with pure integrators.

Even though pure integrators will give stable systems and guaranteed stability when parallel stiffness are added, it would lead to unnecessary gain at low frequency that would modify the damped plant dynamics at low frequency. To avoid that, a second order low pass filter is added at low frequency (2.1).

$$\boldsymbol{K}_{\text{IFF}}(s) = g \cdot \begin{bmatrix} K_{\text{IFF}}(s) & & 0 \\ & \ddots & \\ 0 & & K_{\text{IFF}}(s) \end{bmatrix}, \quad K_{\text{IFF}}(s) = \frac{1}{s} \cdot \frac{\frac{s^2}{\omega_z^2}}{\frac{s^2}{\omega_z^2} + 2\xi_z \frac{s}{\omega_z} + 1} \tag{2.1}$$

The frequency of the second order high pass filter is tuned to be below the frequency of the complex conjugate zero for the highest mass (here at 4 Hz). The overall gain is increased to have some authority on the nano-hexapod modes that we want to damp (Figure 2.3).

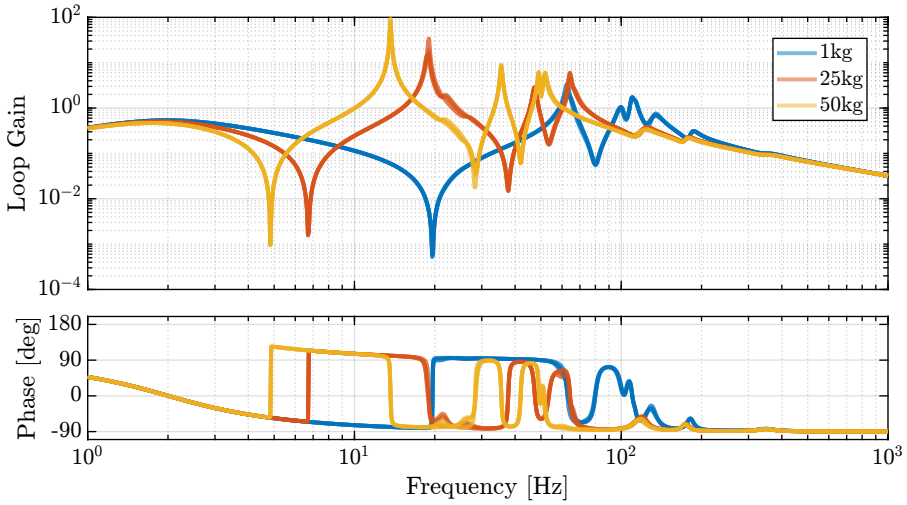

Figure 2.3: Loop gain for the decentralized IFF: $K_{\text{IFF}}(s) \cdot \frac{f_{mi}}{f_i}(s)$

In order to check the stability, root loci for the three payload configurations are computed and shown in Figure 2.4. It is shown that the closed-loop poles are bounded to the left-half plane indicating the good robustness properties of the applied decentralized IFF.

Conclusion

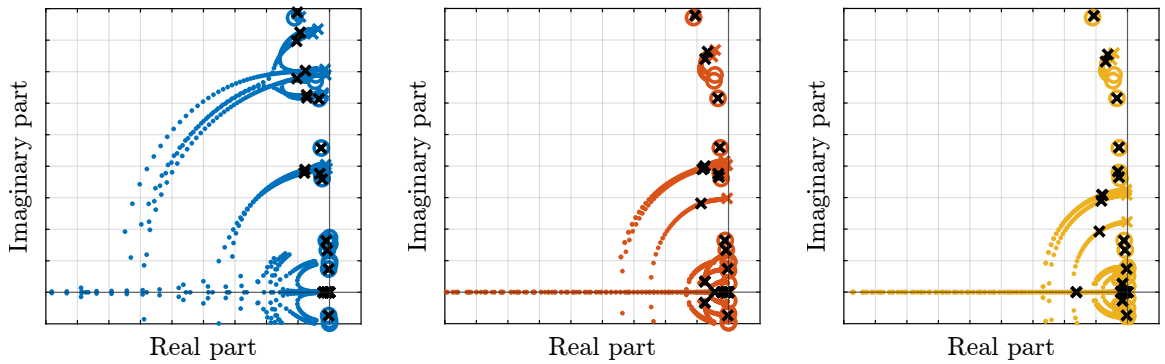

(a) 1 kg **(b)** 25 kg **(c)** 50 kg

Figure 2.4: Measurement of strut flexible modes

3 Centralized Active Vibration Control

Effect of micro-station compliance Compare plant with “rigid” u-station and normal u-station

- Effect of IFF
- Effect of payload mass
- Decoupled plant
- Controller design

From control kinematics:

- Talk about issue of not estimating Rz from external metrology? (maybe could be nice to discuss that during the experiments!)
- Show what happens is Rz is not estimated (for instance supposed equaled to zero =¿ increased coupling)

3.1 HAC Plant

- Effect of rotation: 3.1a Add some coupling at low frequency, but still small at the considered velocity. This is thanks to the relatively stiff nano-hexapod (CF rotating model)
- Effect of payload mass: Decrease resonance frequencies Increase coupling: 3.1b =¿ control challenge for high payload masses
- Other effects such as: Ry tilt angle, Rz spindle position, micro-hexapod position are found to have negligible effect on the plant dynamics. This is thanks to the fact the the plant dynamics is well decoupled from the micro-station dynamics.
- Effect of IFF on the plant 3.2a Modes are well damped Small coupling increase at low frequency
- Benefits of using IFF 3.2b with added damping, the set of plants to be controlled (with payloads from 1kg to 50kg) is more easily controlled. Between 10 and 50Hz, the plant dynamics does not vary a lot with the frequency, whereas without active damping, it would be impossible to design a robust controller with bandwidth above 10Hz that is robust to the change of payload

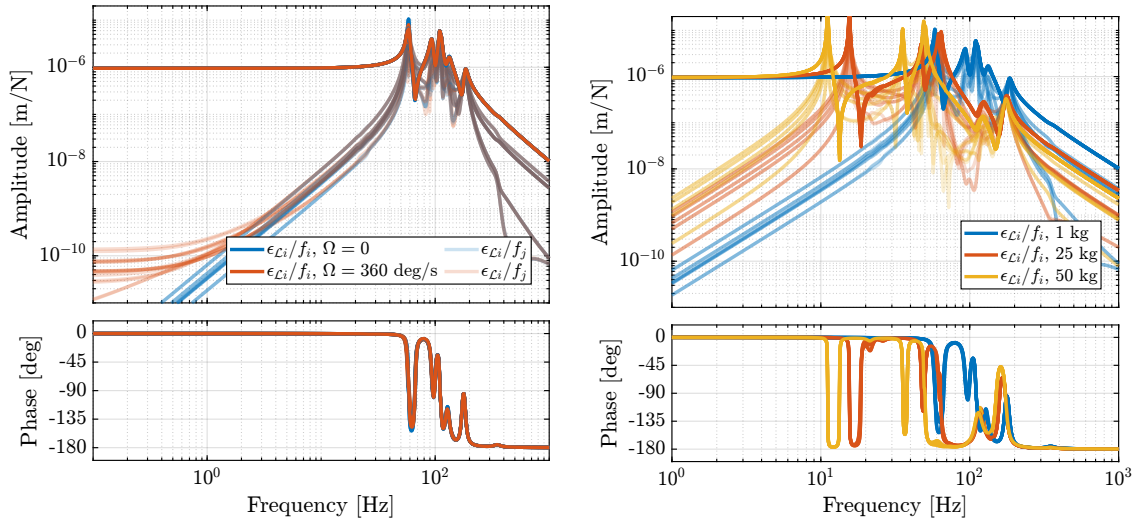

(a) Effect of rotational velocity Ω_z

(b) Effect of payload's mass

Figure 3.1: Effect of the Spindle's rotational velocity on the positioning plant (a) and effect of the payload's mass on the positioning plant (b)

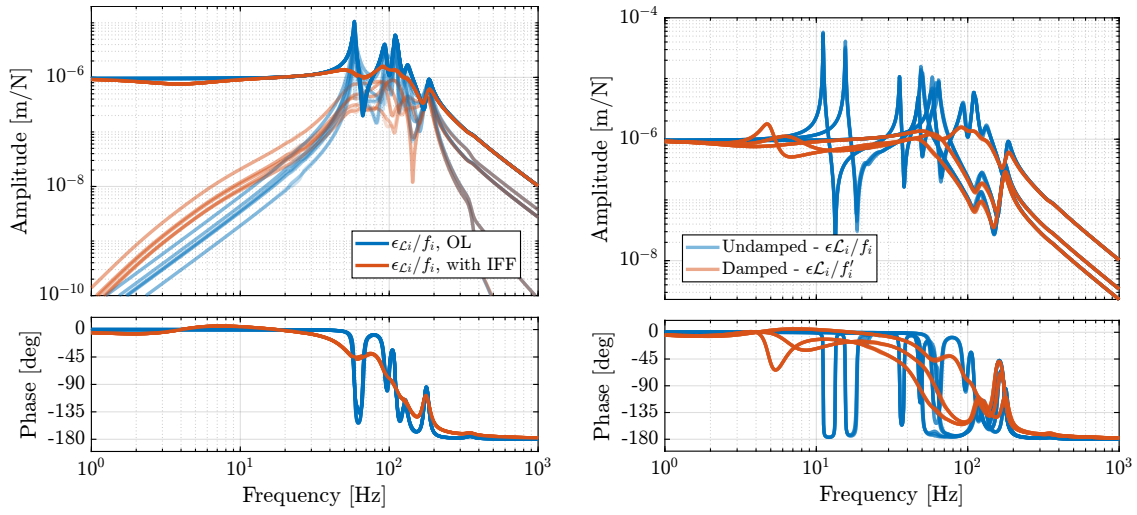

(a) Effect of IFF - $m = 1\,\text{kg}$

(b) Effect of IFF on the set of plants to control

Figure 3.2: Effect of the Spindle's rotational velocity on the positioning plant (a) and effect of the payload's mass on the positioning plant (b)

3.2 Effect of micro-station compliance

Micro-Station complex dynamics has almost no effect on the plant dynamics (Figure 3.3):

- adds some alternating poles and zeros above 100Hz, which should not be an issue for control

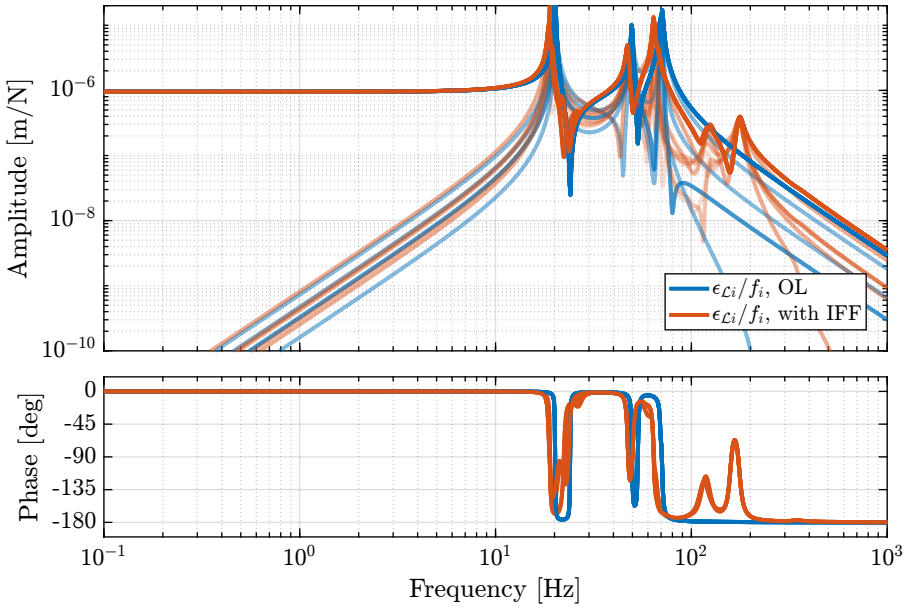

Figure 3.3: Effect of the micro-station limited compliance on the plant dynamics

3.3 Higher or lower nano-hexapod stiffness?

Goal: confirm the analysis with simpler models (uniaxial and 3DoF) that a nano-hexapod stiffness of $\approx 1\,N/\mu m$ should give better performances than a very stiff or very soft nano-hexapod.

- **Stiff nano-hexapod**: uniaxial model: high nano-hexapod stiffness induce coupling between the nano-hexapod and the micro-station dynamics. considering the complex dynamics of the micro-station as shown by the modal analysis, that would result in a complex system to control To show that, a nano-hexapod with actuator stiffness equal to 100N/um is initialized, payload of 25kg. The dynamics from $\boldsymbol{f}$ to $\boldsymbol{\epsilon}_{\mathcal{L}}$ is identified and compared to the case where the micro-station is infinitely rigid (figure 3.4a):
  - Coupling induced by the micro-station: much more complex and difficult to model / predict
  - Similar to what was predicted using the uniaxial model
- **Soft nano-hexapod**: Nano-hexapod with stiffness of 0.01N/um is initialized, payload of 25kg. Dynamics is identified with no spindle rotation, and with spindle rotation of 36deg/s and 360deg/s (Figure 3.4b)
  - Rotation as huge effect on the dynamics: unstable for high rotational velocities, added

coupling due to gyroscopic effects, and change of resonance frequencies as a function of the rotational velocity

– Simple 3DoF rotating model is helpful to understand the complex effect of the rotation =¿ similar conclusion

– Say that controlling the frame of the struts is not adapted with a soft nano-hexapod, but we should rather control in the frame matching the center of mass of the payload, but we would still obtain large coupling and change of dynamics due to gyroscopic effects.

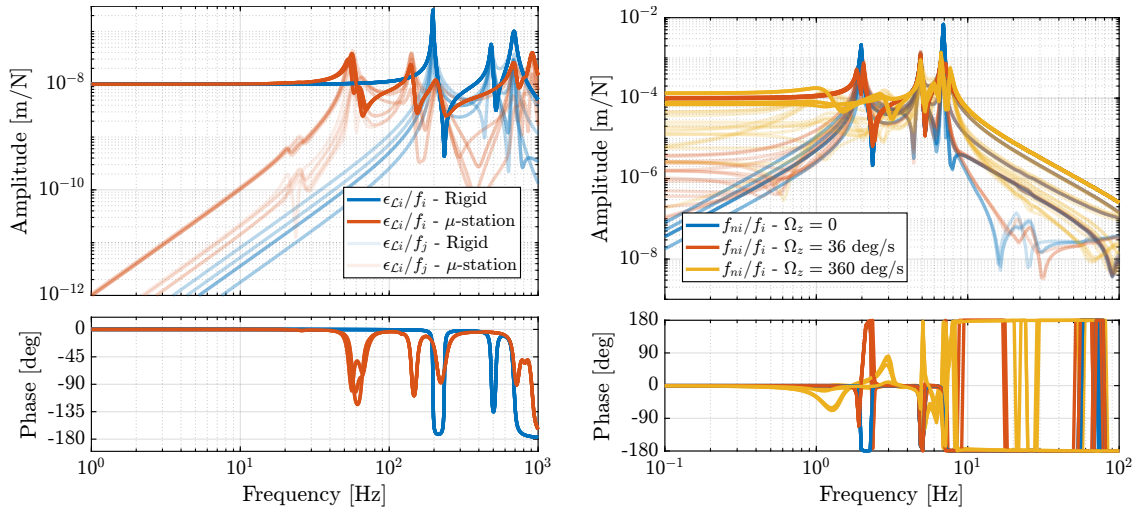

(a) Stiff nano-hexapod - Coupling with the micro-station

(b) Soft nano-hexapod - Effect of Spindle rotational velocity

Figure 3.4: Plant dynamics of a stiff ($k_a = 100\,N/\mu m$) nano-hexapod (a) and of a soft ($k_a = 0.01\,N/\mu m$) nano-hexapod (b)

3.4 Controller design

In this section, a high authority controller is design such that:

- it is robust to the change of payload mass (i.e. is should be stable for all the damped plants of Figure 3.2b)
- it has reasonably high bandwidth to give good performances (here 10Hz)

(3.1)

$$K_{\text{HAC}}(s) = g_0 \cdot \underbrace{\frac{\omega_c}{s}}_{\text{int}} \cdot \underbrace{\frac{1}{\sqrt{\alpha}} \frac{1 + \frac{s}{\omega_c/\sqrt{\alpha}}}{1 + \frac{s}{\omega_c\sqrt{\alpha}}}}_{\text{lead}} \cdot \underbrace{\frac{1}{1 + \frac{s}{\omega_0}}}_{\text{LPF}}, \quad (\omega_c = 2\pi 10\,\text{rad/s},\ \alpha = 2,\ \omega_0 = 2\pi 80\,\text{rad/s}) \tag{3.1}$$

- "Decentralized" Loop Gain: Bandwidth around 10Hz
- Characteristic Loci: Stable for all payloads with acceptable stability margins

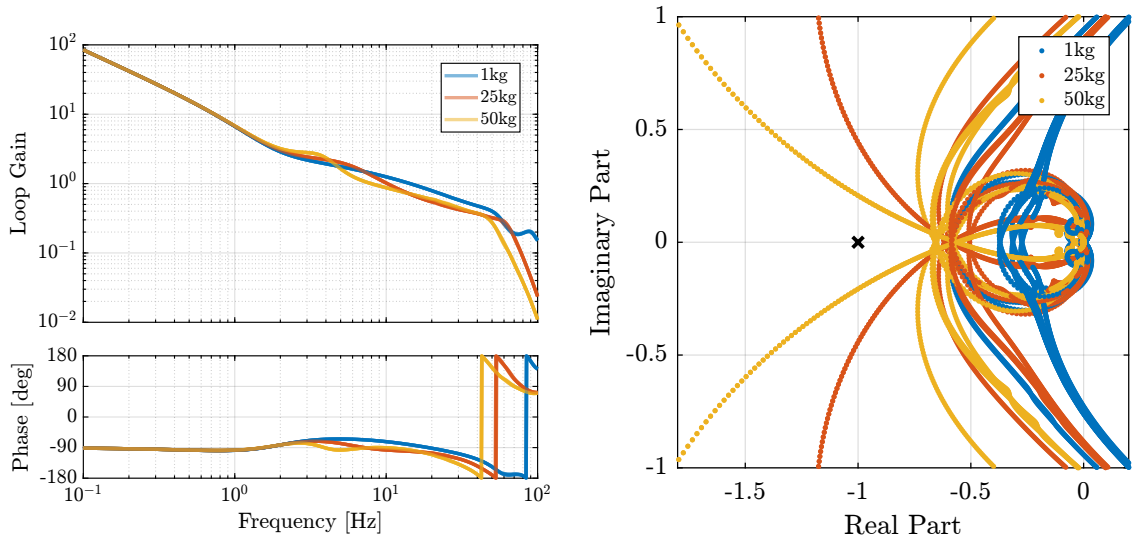

(a) Loop Gain **(b)** Characteristic Loci

Figure 3.5: High Authority Controller - "Diagonal Loop Gain" (a) and Characteristic Loci (b)

3.5 Tomography experiment

- Validation of concept with tomography scans at the highest rotational velocity of $\Omega_z = 360\,\mathrm{deg/s}$
- Compare obtained results with the smallest beam size that is expected with future beamline upgrade: 200nm (horizontal size) x 100nm (vertical size)
- Take into account the two main sources of disturbances: ground motion, spindle vibrations Other noise sources are not taken into account here as they will be optimized latter (detail design phase): measurement noise, electrical noise for DAC and voltage amplifiers, ...

The open-loop errors and the closed-loop errors for the tomography scan with the light sample $1\,kg$ are shown in Figure 3.6.

- Effect of payload mass (Figure 3.7): Worse performance for high masses, as expected from the control analysis, but still acceptable considering that the rotational velocity of 360deg/s is only used for light payloads.

Conclusion

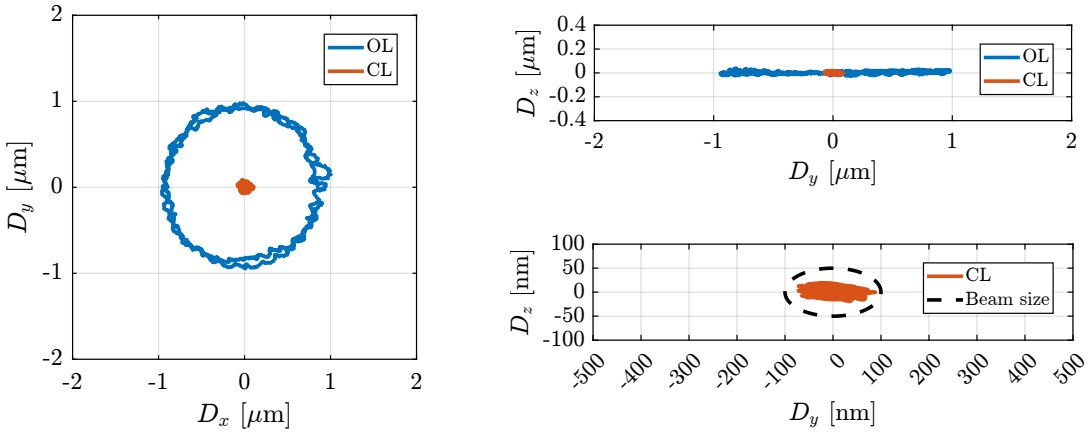

(a) XY plane **(b)** YZ plane

Figure 3.6: Position error of the sample in the XY (a) and YZ (b) planes during a simulation of a tomography experiment at 360 deg/s. 1kg payload is placed on top of the nano-hexapod.

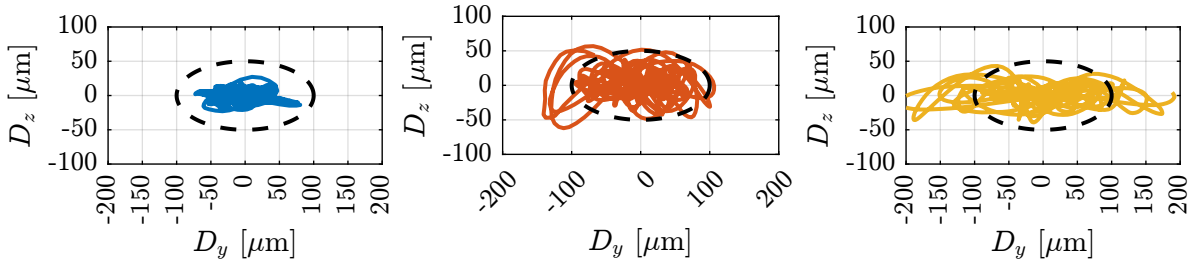

(a) $m = 1\,kg$ **(b)** $m = 25\,kg$ **(c)** $m = 50\,kg$

Figure 3.7: Simulation of tomography experiments - 360deg/s. Beam size shown by dashed black

Conclusion